Microscale receiver operating characteristic analysis of micrometastasis recognition using activatable fluorescent probes indicates leukocyte imaging as a critical factor to enhance accuracy

Bryan Q. Spring
Akilan Palanisami
Tayyaba Hasan

Microscale receiver operating characteristic analysis of micrometastasis recognition using activatable fluorescent probes indicates leukocyte imaging as a critical factor to enhance accuracy

Bryan Q. Spring,[a] Akilan Palanisami,[a] and Tayyaba Hasan[a,b,c,*]
[a]Massachusetts General Hospital and Harvard Medical School, Wellman Center for Photomedicine, Boston, Massachusetts 02114
[b]Massachusetts General Hospital, Department of Dermatology, Boston, Massachusetts 02114
[c]Harvard University and Massachusetts Institute of Technology, Division of Health Sciences and Technology, Cambridge, Massachusetts 02139

Abstract. Molecular-targeted probes are emerging with applications for optical biopsy of cancer. An underexplored potential clinical use of these probes is to monitor residual cancer micrometastases that escape cytoreductive surgery and chemotherapy. Here, we show that leukocytes, or white blood cells, residing in nontumor tissues—as well as those infiltrating micrometastatic lesions—uptake cancer cell-targeted, activatable immunoconjugates nonspecifically, which limits the accuracy and resolution of micrometastasis recognition using these probes. Receiver operating characteristic analysis of freshly excised tissues from a mouse model of peritoneal carcinomatosis suggests that dual-color imaging, adding an immunostain for leukocytes, offers promise for enabling accurate recognition of single cancer cells. Our results indicate that leukocyte identification improves micrometastasis recognition sensitivity and specificity from 92 to 93%—for multicellular metastases >20 to 30 μm in size—to 98 to 99.9% for resolving metastases as small as a single cell. © *2014 Society of Photo-Optical Instrumentation Engineers (SPIE)* [DOI: 10.1117/1.JBO.19.6.066006]

Microscopic deposits of cancer cells missed during cytoreductive surgery frequently contain a subpopulation of cells with either intrinsic or acquired drug-resistance that escape follow-up chemotherapy and stimulate disease recurrence; for example, this is a key characteristic of ovarian cancer.[1–4] A major challenge in oncology is the lack of imaging modalities capable of detecting or monitoring these residual microscopic tumors.[5–7] Inspired by elegant reports of microscopic tumor visualization using intravital microscopy to study basic cancer biology,[8] *in vivo* histopathology, and molecular imaging using microendoscopy[9–16] as well as activatable fluorescent[17–21] and photodynamic probes,[22,23] we previously reported quantitative, repeated, and longitudinal monitoring of cancer micrometastases *in vivo* within select regions of the peritoneal cavity using a cancer cell-targeted, activatable, and photocytotoxic immunoconjugate integrated with fluorescence microendoscopy.[24] The activatable immunoconjugate[25,26] targets cancer cells overexpressing the epidermal growth factor receptor (EGFR) and serves dual functions as an imaging probe and a combinational therapeutic agent,[24,27] enabling selective destruction of disseminated cancer micrometastastes upon wide-field, near-infrared irradiation—a new mode of photoimmunotherapy[28–30] termed tumor-targeted, activatable photoimmunotherapy.[24]

The activatable immunoconjugate (Cet-BPD) is composed of cetuximab, an anti-EGFR monoclonal antibody (MAb) that targets cancer cells overexpressing EGFR, loaded with benzoporphyrin derivative (BPD) molecules, a U.S. Food and Drug Administration-approved photocytotoxic chromophore that undergoes electronic excited state quenching upon antibody conjugation.[25] In this approach, both the photodynamic and fluorescence components of the immunoconjugate become de-quenched (activated) upon cellular internalization and processing.[24,25] Because cancer cells overexpressing the target surface molecules take up the immunoconjugates more efficiently, this targeted activation occurs predominantly within tumors and enhances tumor selectivity (based on extensive imaging and phototoxicology studies comparing immunoconjugates with low- and high-quenching efficiencies).[24] These studies, and the present study, were performed in a clinically motivated mouse model of human ovarian carcinomatosis previously established in our laboratory with gynecologic oncologists.[31] In this orthotopic xenograft model, athymic Swiss female Nu/Nu mice (20 to 25 g and six- to eight-weeks old; Cox Breeding Laboratories, Cambridge, Massachusetts) are injected intraperitoneally (i.p.) with 16×10^6 NIH:OVCAR5 (human ovarian cancer) cells in 2 mL phosphate-buffered saline, leading to disseminated tumor nodules studding the peritoneal organs and surfaces. All animal experiments were conducted according to Massachusetts General Hospital Institutional Animal Care and Use Committee guidelines. Conjugates of BPD and mAb (Cet) were prepared as described previously[24,25] and administered at $2 \text{ mg} \cdot \text{kg}^{-1}$ body weight BPD (1.4 mg cetuximab). All injections were done i.p. in 1 mL of sterile phosphate-buffered saline. The cetuximab dose (1.4 mg) is equivalent to $\sim$180 $\text{mg} \cdot \text{m}^{-2}$ and near the clinical cetuximab dose of 250 to 400 $\text{mg} \cdot \text{m}^{-2}$.

*Address all correspondence to: Tayyaba Hasan, E-mail: thasan@mgh.harvard.edu

To examine the microscopic localization of activated immunoconjugates, we performed histopathologic examination of tissue biopsies coregistered with *in vivo* fluorescence microendoscopy images, and we performed confocal fluorescence microscopy of freshly excised tissues from the peritoneal cavity. Our prior results indicated 90% sensitivity and 90% specificity for tumors as small as 30 μm (a small cluster of cells) using monochromatic fluorescence detection of the activatable immunoconjugate.[24] However, both immunofluorescence microscopy and histopathology suggested that a subpopulation of CD45+ (leukocyte common antigen or protein tyrosine phosphatase, receptor type, C) leukocytes uptake and activate the immunoconjugate and that this source of nonspecific probe activation limits the resolution of accurate micrometastasis recognition and quantitative monitoring post-treatment.[24]

In the present study, we hypothesized that CD45 imaging can supplement activatable immunoconjugate imaging to enhance the accuracy and resolution of micrometastasis recognition. CD45+ cells, including macrophages residing in tissue, express Fc-γ-receptors that react with the Fc portion of MAbs to promote engulfment and phagocytosis as a mechanism of probe catabolism and elimination from the body.[32] Here, we show that dual color imaging, adding an immunostain for CD45+ leukocytes—which can uptake activatable probes nonspecifically—can increase both the sensitivity and specificity to 98% for recognition of single cancer cells.
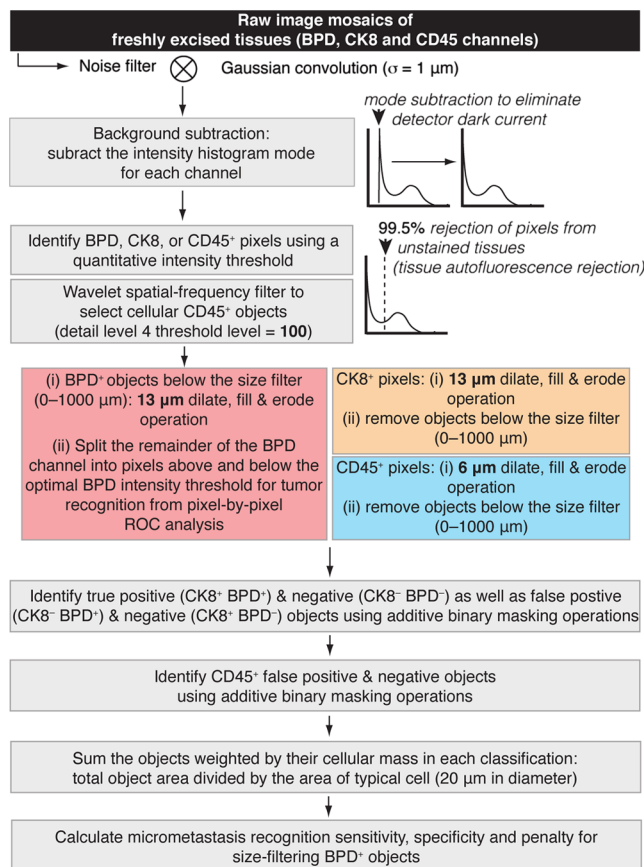
To test this concept of immune cell imaging in combination with activatable probes, we collected a series of confocal fluorescence image mosaics of freshly excised tissues from the mouse model of metastatic ovarian cancer prior to [day 0, no-tumor control; Fig. 1(a)] and at various days following
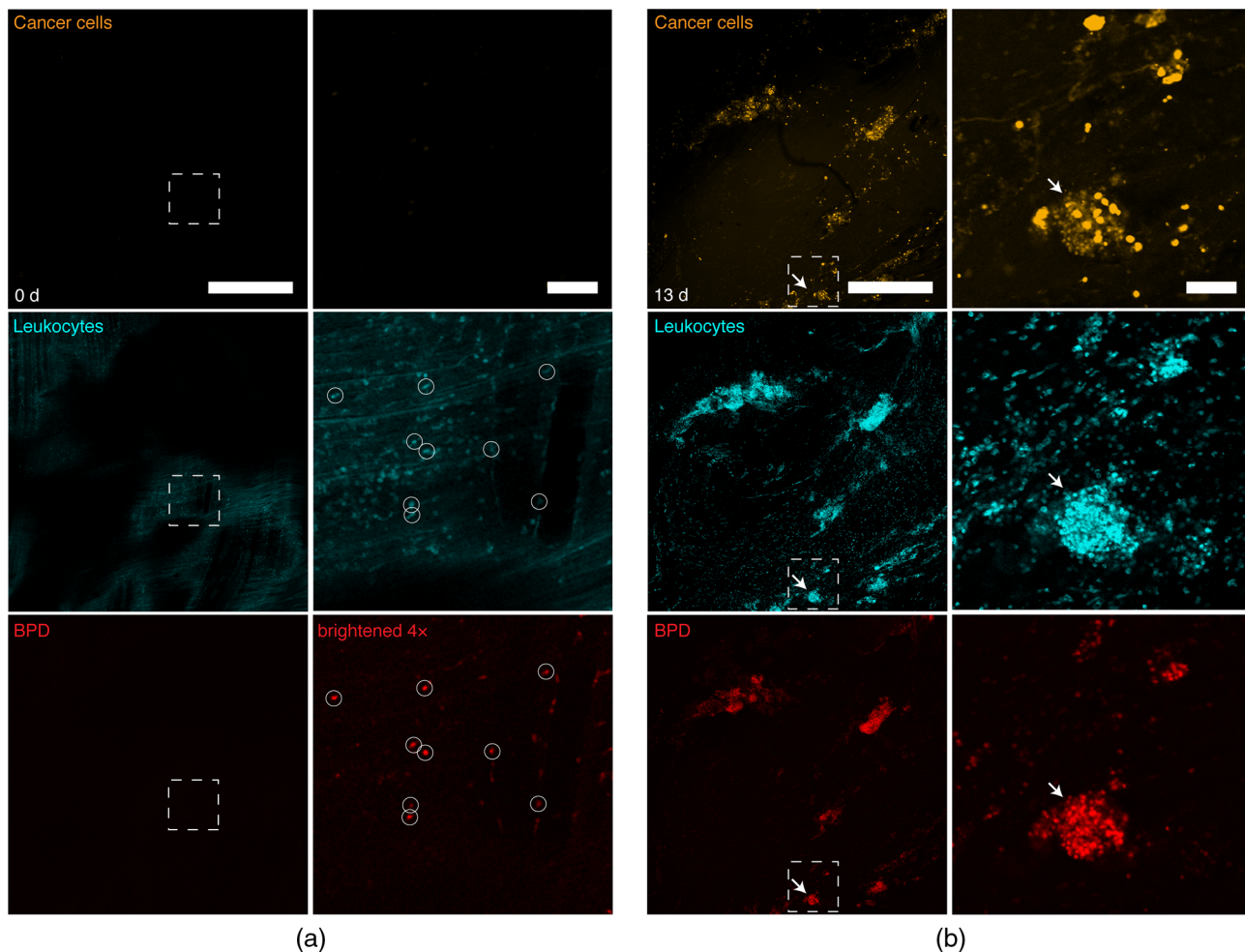
Fig. 1 (a) Confocal fluorescence image mosaics (left) and insets (right) of freshly excised tissue from control no-tumor mice. Human ovarian cancer cells (orange; antihuman cytokeratin 8 immunostain) are not found in these control mice. The locations of mouse leukocytes (cyan; antimouse CD45 immunostain) are shown for comparison with benzoporphyrin derivative (BPD) fluorescence (red; activated Cet-BPD immunoconjugates administered *in vivo*). Circles indicate leukocytes with activated BPD fluorescence (brightened 4× for visibility). (b) Confocal fluorescence image mosaics (left) and insets (right) of freshly excised tissue from epithelial ovarian cancer mice with disseminated, peritoneal micrometastatic disease. Note that leukocytes are an important cell population within the tumor microenvironment, are known to infiltrate cancer metastases, and often compose a large fraction of the tumor mass.[4] Arrows indicate a micrometastasis composed of ovarian cancer cells (orange) as well as tumor-infiltrating leukocytes (cyan) with activated BPD fluorescence (red). Scale bars are 1 mm in (a) and (b) (left) and 100 μm in (a) and (b) (right).

tumor inoculation (days 3, 9, and 13; Fig. 1(b)] following administration of the Cet-BPD activatable immunoconjugate. BPD fluorescence corresponding to cancer cells and leukocytes is apparent in the resulting confocal image mosaics (Fig. 1). We designed two microscopic-resolution receiver operating characteristic (ROC) analyses using an antihuman cytokeratin 8 MAb (CK8; clone LP3K, R&D Systems, Minneapolis, Minnesota) specific for human epithelial cancer cells[24] as a gold standard marker: (1) a pixel-by-pixel analysis[24] and (2) an object-by-object analysis (Fig. 2), where pixels are grouped into fluorescent objects and weighted as the object area normalized by the typical area of a single cell (diameter = 20 μm).

Following i.p. injection of Cet-BPD immunoconjugates (8 h post injection), freshly excised peritoneal wall specimens were immediately blocked (Dako Protein Block, Carpinteria, California), followed by immunofluorescence staining (10 to 16 μg/mL for each MAb), rinsed with fresh phosphate-buffered saline, and mounted on a coverslip bottom dish (MaTek, Ashland, Massachusetts). MAb-Alexa Fluor (AF) dye conjugates for *ex vivo* immunofluorescence staining were prepared using MAb-labeling kits (Life Technologies, Grand Island, New York): anti-human CK8 and anti-mouse CD45 (clone 30-F11, R&D Systems) were conjugated to AF647 and AF488, respectively. Imaging was performed with an Olympus FV1000 confocal microscope with a 10× objective. Excitation of BPD, AF488, and AF647 was carried out using 405-, 488-, and 635-nm lasers,

respectively. Lasers were scanned sequentially to reduce channel crosstalk. The laser, photomultiplier tube detector, and pinhole settings were kept constant for each fluorophore. ROC analyses were performed using a custom, batch-processing Matlab (Mathworks, Natick, Massachusetts) routine. The tumor classification tests used objective intensity thresholds set to reject 99.5% of the background signal from the CK8 channel. That is, unstained control tissues were used to characterize and set quantitative thresholds to reject autofluorescence background (set to reject 99.5% of the non-Gaussian background intensity distribution[24]). For object selection in the CD45 channel (AF488, which overlaps strongly with autofluorescence), we developed a wavelet multiresolution decomposition[33] (essentially band pass spatial frequency filtering) algorithm to select CD45$^+$ cellular objects using the "wavedec2" and "wrcoef" functions with biorthogonal wavelets (bior3.7; Matlab Wavelet Toolbox). This routine calculates the absolute pixel values of image spatial frequencies band passed into detail level 4 and applies an intensity threshold (threshold level = 100) to select cellular objects.

In the first ROC analysis to assess the cancer cell-selectivity of Cet-BPD activation, we performed pixel-by-pixel tumor classification based on a Cet-BPD fluorescence intensity threshold from which we determined Cet-BPD sensitivity (fraction of cancer cell pixels correctly identified) and specificity (1−fraction of cancer cell pixels incorrectly identified). The optimal BPD intensity threshold attained 92 to 93% sensitivity and specificity (ROC area under the curve = 0.96) for micrometastases as small as 20 to 30 μm [Figs. 3(a) and 3(b)], as reported previously.[24] For this analysis, we applied a balanced 21 μm dilate, fill and erode binary image operations using the "bwmorph" and "imfill" functions (Matlab) to connect intercellular spaces of multicellular tumor objects. Size filtering of fluorescent objects in each channel was performed using the "bwareaopen" function. In addition, we calculated a penalty for size filtering potential BPD$^+$ objects (above the 99.5% background rejection intensity threshold) below the 20 to 30 μm limit. The penalty is calculated as the percentage of BPD$^+$ objects or pixels removed by the size filter, indicating that a substantial number of sub-20-μm objects are missed by this analysis [Fig. 3(c)]. Thus, size-filtering objects below the 20 to 30 μm limit provides an optimized algorithm for analyzing monochromatic fluorescence imaging of multicellular micrometastatic nodules, but there is great potential for dual-color fluorescence imaging—combining cancer cell-targeted activatable immunoconjugate with anti-CD45 MAb imaging—to further increase the accuracy and resolution of the smallest (i.e., single cell) micrometastases.

To explore the potential of dual-color imaging, we next added a third classification (false positives due to leukocytes residing in nontumor tissue, or cancer cell pixels incorrectly identified as tumor corresponding to CD45$^+$ false positive pixels). The CD45$^+$ false positive classification has no effect on the pixel-by-pixel ROC analysis due to the relatively small number of CD45$^+$ nontumor pixels, which suggests that an object-by-object analysis is more appropriate. As described above, we weighted objects to their cellular mass (units of number of cells estimated from the object area) in order to equally weight true positive and true negative objects (contiguous groups of pixels correctly identified as tumor or correctly identified as nontumor) with false positive and false negative objects.

A noteworthy complication for object-by-object ROC analysis (with object assignment among three or more classes) is the potential to fragment objects during multiplicative binary
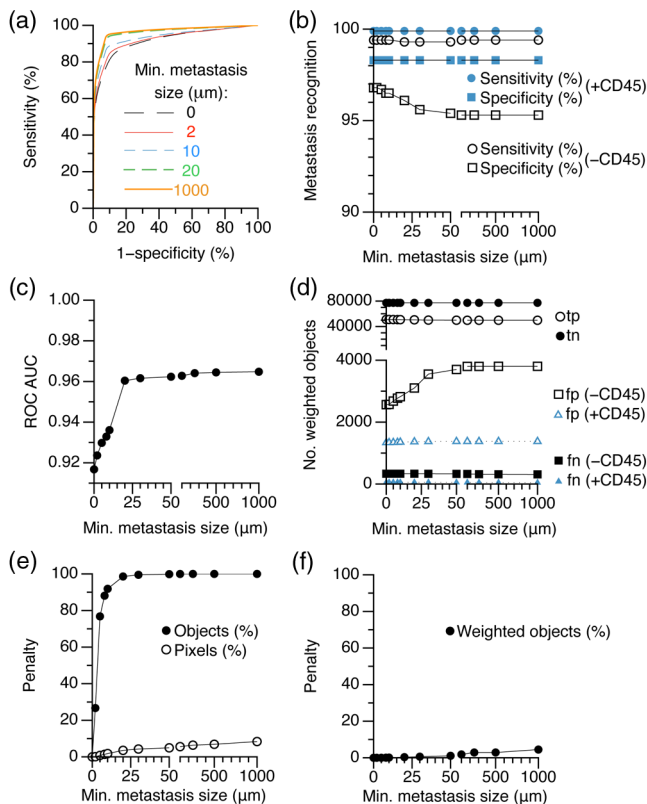

Fig. 2 Image analysis workflow for weighted object, dual-color micrometastasis recognition. Note that the free parameters and their values are highlighted in bold font. The single-color, pixel-by-pixel receiver operating characteristic (ROC) analysis has been described previously[24] and is similar to this workflow but does not use the CD45 channel or weighted objects.

Fig. 3 (a) A pixel-by-pixel ROC analysis of micrometastasis recognition using Cet-BPD—as a function of the minimum metastasis size. (b) The pixel-by-pixel ROC area under the curve for various minimum metastasis sizes. (c) The percentage of potential tumor objects and pixels missed by size filtering the ROC analysis (i.e., a penalty for limiting the ROC analysis to a minimum micrometastasis size). (d) Sensitivity and specificity for tumor recognition grouping pixels into individual, fluorescent objects (i.e., quantitative thresholds are used to reject pixels below a threshold that rejects 99.5% of background[24]) weighted by their area normalized to that of a single cell (diameter = 20 μm). (e) Number of true (tp) and false positive (fp) weighted tumor objects as well as true (tn) and false negative (fn) weighted tumor objects. In (d) and (e), leukocyte (+CD45) imaging removes 48% of fp weighted objects to improve micrometastasis recognition compared to imaging only Cet-BPD. In addition to nonspecific Cet-BPD uptake, leukocytes also uptake the anti-CK8 antibody (albeit infrequently);therefore, CD45 imaging also eliminates a fraction of the fn (CD45+ CK8+ BPD−) objects. Note that CD45 imaging has a negligible effect on the number of tp and tn weighted objects (omitted for clarity). (f) The percentage of potential tumor objects missed by size filtering the object-by-object ROC analysis. Results $n = 12$ mice (296 fields) in (a) to (c), and 4 mice (131,110 weighted objects) in (d) to (f).

masking operations. That is, binary masks calculated by intensity thresholding the raw image channels are normally multiplied to select colocalized objects and assign them to specific classes. However, this approach can split objects in complex images involving multiple channels and classifications. To prevent object fragmentation and to avoid splitting objects among different classifications, we used additive masking operations. This was accomplished using the "bwconncomp," "regionprops," "labelmatrix," "find," and "ismember" functions (Matlab) to assign contiguous BPD+ objects (following a 13 micron, balanced dilate, fill and erode binary image operation) to tumor, nontumor leukocytes, or nontumor (and nonleukocyte) classifications. Binary mask addition sets pixels within overlapping objects to 2, such that the mean intensity of the object is >1.

Objects with mean intensity >1 can then be found (using the "find" and "ismember" functions) and then the entire object can be assigned to the corresponding class (e.g., true positive). Similarly, objects with a mean intensity equal to 1 can be assigned to the opposing classification (e.g., false positive) without object fragmentation into multiple classifications. This strategy is less sensitive to chromatic aberrations and other sources of pixel color shift, as well as decreasing sensitivity to out-of-focus shadowing effects surrounding multilayer tumor objects.

The free parameters for these analyses (the wavelet threshold and the dilate-fill-erode distance) were tuned manually on a pair of test images (one nontumor control and one tumor biopsy), and then the entire set of image mosaics (eight tissue biopsies) were batch processed.

The results of the weighted object-by-object ROC analysis were calculated with (+CD45) and without (−CD45) the leukocyte channel using the optimal BPD intensity threshold identified by the pixel-by-pixel ROC analysis (optimal BPD intensity threshold = 69 on a 12-bit scale). Dual-color Cet-BPD and CD45 imaging had a marked impact on the false positive rate, improving the specificity of micrometastasis recognition [Figs. 2(d) and 2(e)]. The dual-color, object-by-object ROC analysis indicates 99.9% sensitivity and 98.3% specificity for micrometastases as small as a single cell [no size filtering, 0% penalty; Figs. 3(d) to 3(f)]. Note that almost all of the unweighted objects are <20 μm in size; therefore, the penalty approaches 100% [Fig. 3(c)]. In contrast, weighting the objects by the number of cells they contain decreases the penalty for size filtering small objects. However, size filtering is not needed and the penalty is zero when CD45 imaging is implemented [Figs. 3(d) to 3(f)].

In summary, molecular-targeted probes are emerging for performing minimally invasive *in vivo* microscopy with applications in oncology. An underexplored potential clinical use of these probes, in combination with fluorescence microendoscopy, is minimally invasive, repeated and quantitative monitoring of cancer micrometastases in select sites is known to frequently harbor residual disease. CD45 (a leukocyte surface antigen) is a useful marker for identifying immune cells that uptake antibodies nonspecifically (e.g., macrophages)[26] and removing these cells from analysis of micrometastases using cancer cell-targeted, activatable immunoconjugates. Multicolor approaches offer promise for treating and monitoring drug-resistant micrometastases presently invisible to clinicians with a sensitivity and specificity of ~98% for untreated tumors as small as a single cancer cell. Such an approach will also be of particular importance for monitoring micrometastasis destruction, to distinguish residual, tumor-associated inflammatory cells from residual cancer cells.

We anticipate that the overall approach of leukocyte imaging will be translated for use in humans and will be impactful for reducing false positives by identifying the immune cell uptake. In addition, the ROC analysis assay developed here has potential for translation to study cancer recognition using targeted molecular probes in human tissues. However, in the xenograft mouse model of epithelial ovarian cancer (EOC), we leveraged use of an antihuman CK8 probe that specifically binds human, but not mouse, protein to realize a high-fidelity gold standard marker for the human epithelial cancer cells. (In contrast, cetuximab binds both mouse and human EGFR.[24]) Developing such a gold standard in human tissues will require some thought and further development. Furthermore, although EGFR is highly expressed by some tumors, it is unlikely that a single molecular marker can

be used to address inter- and intrapatient tumor heterogeneity and cancer cell clonal diversity; thus, new creative approaches will be needed to address multiple potential tumor biomarkers in human patients. Moreover, study of additional tissue types beyond the peritoneal tissues examined here is also warranted.

Of equal importance to probe and image analysis design is the development of clinical microendoscopy technology capable of more comprehensive samplings of micrometastatic burden. Elegant reports of comprehensive volumetric imaging of entire luminal organs have been accomplished, for instance, by rotary pull-back of tethered capsule probes through the gastrointestinal tract.[34] However, the microscopic field-of-view does impose practical limits on sampling the entire micrometastatic burden in complex anatomical sites (e.g., the peritoneal cavity). Fiber-scanning microendoscope probes[35] as well as multiresolution, foveated lens systems[36] can expand the field-of-view to enable efficient scanning of cavities and organs comparable to conventional endoscopy but with ultrathin probes and microscopic resolution. Furthermore, a number of advanced microscopy techniques, including multiphoton excitation[37] and super-resolution imaging,[38,39] have potential to or have already improved the imaging depth and resolution of microendoscopy.

Acknowledgments

References

1. H. Naora and D. J. Montell, "Ovarian cancer metastasis: integrating insights from disparate model organisms," *Nat. Rev. Cancer* **5**(5), 355–366 (2005).
2. R. C. Bast, B. Hennessy, and G. B. Mills, "The biology of ovarian cancer: new opportunities for translation," *Nat. Rev. Cancer* **9**(6), 415–428 (2009).
3. E. Lengyel, "Ovarian cancer development and metastasis," *Am. J. Pathol.* **177**(3), 1053–1064 (2010).
4. D. A. Leinster et al., "The peritoneal tumour microenvironment of high-grade serous ovarian cancer," *J. Pathol.* **227**(2), 136–145 (2012).
5. K. Pantel, C. Alix-Panabières, and S. Riethdorf, "Cancer micrometastases," *Nat. Rev. Clin. Oncol.* **6**(6), 339–351 (2009).
6. A. Gadducci et al., "Surveillance procedures for patients treated for epithelial ovarian cancer: a review of the literature," *Int. J. Gynecol. Cancer* **17**(1), 21–31 (2007).
7. M. Soussan et al., "Comparison of FDG-PET/CT and MR with diffusion-weighted imaging for assessing peritoneal carcinomatosis from gastrointestinal malignancy," *Eur. Radiol.* **22**(7), 1479–1487 (2012).
8. S. A. Gerber et al., "Preferential attachment of peritoneal tumor metastases to omental immune aggregates and possible role of a unique vascular microenvironment in metastatic survival and growth," *Am. J. Pathol.* **169**(5), 1739–1752 (2006).
9. F. Lüdicke et al., "Photodynamic diagnosis of ovarian cancer using hexaminolaevulinate: a preclinical study," *Br. J. Cancer* **88**(11), 1780–1784 (2003).
10. D. Yelin et al., "Three-dimensional miniature endoscopy," *Nature* **443**(7113), 765 (2006).
11. P.-L. Hsiung et al., "Detection of colonic dysplasia in vivo using a targeted heptapeptide and confocal microendoscopy," *Nat. Med.* **14**(4), 454–458 (2008).
12. W. Zhong et al., "In vivo high-resolution fluorescence microendoscopy for ovarian cancer detection and treatment monitoring," *Br. J. Cancer* **101**(12), 2015–2022 (2009).
13. P. Kim et al., "In vivo wide-area cellular imaging by side-view endomicroscopy," *Nat. Methods* **7**(4), 303–305 (2010).
14. R. John et al., "In vivo magnetomotive optical molecular imaging using targeted magnetic nanoprobes," *Proc. Natl. Acad. Sci. U. S. A.* **107**(18), 8085–8090 (2010).
15. R. M. Williams et al., "Strategies for high-resolution imaging of epithelial ovarian cancer by laparoscopic nonlinear microscopy," *Transl. Oncol.* **3**(3), 181–194 (2010).
16. M. C. Pierce et al., "A pilot study of low-cost, high-resolution microendoscopy as a tool for identifying women with cervical precancer," *Cancer Prev. Res. (Phila)* **5**(11), 1273–1279 (2012).
17. R. Weissleder et al., "In vivo imaging of tumors with protease-activated near-infrared fluorescent probes," *Nat. Biotechnol.* **17**(4), 375–378 (1999).
18. E. S. Olson et al., "Activatable cell penetrating peptides linked to nanoparticles as dual probes for in vivo fluorescence and MR imaging of proteases," *Proc. Natl. Acad. Sci. U. S. A.* **107**(9), 4311–4316 (2010).
19. Y. Urano et al., "Selective molecular imaging of viable cancer cells with pH-activatable fluorescence probes," *Nat. Med.* **15**(1), 104–109 (2009).
20. M. Ogawa et al., "In vivo target-specific activatable near-infrared optical labeling of humanized monoclonal antibodies," *Mol. Cancer Ther.* **8**(1), 232–239 (2009).
21. H. Lee et al., "Near-infrared pH-activatable fluorescent probes for imaging primary and metastatic breast tumors," *Bioconjug. Chem.* **22**(4), 777–784 (2011).
22. G. Zheng et al., "Photodynamic molecular beacon as an activatable photosensitizer based on protease-controlled singlet oxygen quenching and activation," *Proc. Natl. Acad. Sci.* **104**(21), 8989–8994 (2007).
23. J. F. Lovell et al., "Activatable photosensitizers for imaging and therapy," *Chem. Rev.* **110**(5), 2839–2857 (2010).
24. B. Q. Spring et al., "Selective treatment and monitoring of disseminated cancer micrometastases in vivo using dual-function, activatable immunoconjugates," *Proc. Natl. Acad. Sci. U.S.A.* **111**(10), E933–E942 (2014).
25. M. D. Savellano, "Targeting cells that overexpress the epidermal growth factor receptor with polyethylene glycolated BPD verteporfin photosensitizer immunoconjugates," *Photochem. Photobiol.* **77**(4), 431–439 (2003).
26. M. D. Savellano and T. Hasan, "Photochemical targeting of epidermal growth factor receptor: a mechanistic study," *Clin. Cancer Res.* **11**(4), 1658–1668 (2005).
27. A. O. Abu-Yousif et al., "Epidermal growth factor receptor-targeted photosensitizer selectively inhibits EGFR signaling and induces targeted phototoxicity in ovarian cancer cells," *Cancer Lett.* **321**(2), 120–127 (2012).
28. D. Mew et al., "Photoimmunotherapy: treatment of animal tumors with tumor-specific monoclonal antibody-hematoporphyrin conjugates," *J. Immunol.* **130**(3), 1473–1477 (1983).
29. A. R. Oseroff et al., "Antibody-targeted photolysis: selective photodestruction of human T-cell leukemia cells using monoclonal antibody-chlorin e6 conjugates," *Proc. Natl. Acad. Sci.* **83**(22), 8744–8748 (1986).
30. B. A. Goff, M. Bamberg, and T. Hasan, "Photoimmunotherapy of human ovarian carcinoma cells ex vivo," *Cancer Res.* **51**(18), 4762–4767 (1991).
31. K. L. Molpus et al., "Characterization of a xenograft model of human ovarian carcinoma which produces intraperitoneal carcinomatosis and metastases in mice," *Int. J. Cancer* **68**(5), 588–595 (1996).
32. W. Wang, E. Q. Wang, and J. P. Balthasar, "Monoclonal antibody pharmacokinetics and pharmacodynamics," *Clin. Pharmacol. Ther.* **84**(5), 548–558 (2008).
33. S. G. Mallat, "A theory for multiresolution signal decomposition: the wavelet representation," *IEEE Trans. Pattern Anal. Mach. Intell.* **11**(7), 674–693 (1989).
34. M. J. Gora et al., "Tethered capsule endomicroscopy enables less invasive imaging of gastrointestinal tract microstructure," *Nat. Med.* **19**(2), 238–240 (2013).
35. C. M. Lee et al., "Scanning fiber endoscopy with highly flexible, 1 mm catheterscopes for wide-field, full-color imaging," *J. Biophoton.* **3**(5–6), 385–407 (2010).
36. N. Hagen and T. S. Tkaczyk, "Foveated endoscopic lens," *J. Biomed. Opt.* **17**(2), 021104 (2012).
37. M. T. Myaing, D. J. MacDonald, and X. Li, "Fiber-optic scanning two-photon fluorescence endoscope," *Opt. Lett.* **31**(8), 1076–1078 (2006).
38. F. C. Zanacchi et al., "Live-cell 3D super-resolution imaging in thick biological samples," *Nat. Methods* **8**(12), 1047–1049 (2011).
39. P. Bianchini et al., "Single-wavelength two-photon excitation-stimulated emission depletion (SW2PE-STED) superresolution imaging," *Proc. Natl. Acad. Sci. U.S.A.* **109**(17), 6390–6393 (2012).

Biographies of the authors are not available.